JOURNAL OF AIRCRAFT
Vol. 31, No. 3, May–June 1994

Unsteady Aerodynamic Characteristics of a Dual-Element Airfoil

Ismail H. Tuncer*
Naval Postgraduate School, Monterey, California 93943
and
Lakshmi N. Sankar†
Georgia Institute of Technology, Atlanta, Georgia 30332

Unsteady aerodynamic behavior and load characteristics of a VR-7 slat/airfoil combination oscillating sinusoidally between 5–25 deg have been studied. The unsteady, compressible Navier-Stokes equations are solved on a multiblock grid using an approximate factorization finite difference scheme. In the case of a single airfoil, a massive flow separation and formation of a strong vortex is observed. The vortex-induced suction and the shedding of the vortex into the wake is responsible for high aerodynamic loads and the subsequent stall of the airfoil. In the case of a slat/airfoil combination, the suction peak at the leading edge of the airfoil is reduced significantly in comparison to the single airfoil. Flow separation is confined to the trailing edge of the main airfoil, and the formation of a strong vortical structure is not observed. The slat/airfoil combination does not experience a massive flow separation, and the aerodynamic lift does not undergo the characteristic deep dynamic stall hysteresis loops.

Introduction

IN recent years, there has been an increased interest in exploiting the large unsteady lift generated by wings during pitch-up to enhance the maneuver capabilities of fighter aircraft. Generation of high unsteady lift without the adverse effects of dynamic stall is also a critical design consideration in helicopters. The unsteady loads generated during the dynamic stall of helicopter blades limit the flight speed and reduce maneuverability.

Slats are currently being used in fighter aircraft primarily to enhance takeoff and landing performance. There is a need to investigate whether the use of those devices may be used to enhance the lift generated during pitch-up maneuvers and postpone stall. In helicopter applications, slats are almost never used because of the mechanical complexity and weight considerations. Nevertheless, they may provide improved maneuverability and increase forward flight speed achievable. Work is needed to understand the dynamic lift generation characteristics of dual-element (slat/airfoil) configurations.

Dynamic stall characteristics of airfoils undergoing high amplitude pitching motions and mechanisms to delay or suppress dynamic stall have been studied experimentally as well as numerically by many researchers in the last decade.[1–4] McCroskey et al.[1] conducted an extensive experimental study on dynamic stall characteristics of several airfoils. They have observed that deep dynamic stall is rather insensitive to airfoil profile, Reynolds number, and flow Mach number, but it is a strong function of the reduced frequency of the pitching motion and the maximum angle of attack. In a later study, Carr and McAlister[2] observed that a leading-edge slat postpones the dynamic stall angle well beyond that of the single airfoil. They hypothesized that this behavior is attributable to the shifting of the flow acceleration onto the slat from the main airfoil. Also, the formation of the leading-edge vortex may be suppressed due to the energizing effect of the vortical wake of the slat on the boundary layer of the main airfoil.

In earlier numerical studies of multielement airfoils, inviscid flow approximations using panel methods[5] or solving potential/Euler flow equations[6] were employed. Recently, Wang[7] investigated high angle-of-attack, separated flows around a VR-7 slat/airfoil combination by solving a velocity-vorticity formulation of the incompressible Navier-Stokes equations.

In this study, dynamic stall characteristics of a VR-7 airfoil with and without a leading-edge slat are investigated using an unsteady, compressible Navier-Stokes solver. In the past, several versions of this solver have been employed successfully to compute subsonic and transonic, steady and unsteady, viscous flows past such diverse configurations as helicopter rotors, high-speed propellers, and fighter wing and bodies.[4,8,9] For investigating flowfields around multielement airfoils, the computational domain is divided into blocks to facilitate the discretization. The Navier-Stokes solver then sweeps the computational blocks. The flow is assumed to be fully turbulent. The computed results are analyzed through a study of computed surface pressure distributions, unsteady lift vs angle of attack behavior, and instantaneous mass-flux contours.

Unsteady Navier-Stokes Equations

The unsteady flowfields around oscillating airfoils is modeled by the Reynolds-averaged, full Navier-Stokes equations. The well-known, conservative form of these equations in an inertial Cartesian coordinate system reads as follows:

$$\boldsymbol{q}_t + \boldsymbol{F}_x + \boldsymbol{G}_y = \boldsymbol{R}_x + \boldsymbol{S}_y \tag{1}$$

where $\boldsymbol{q}$ is the conservative flow variables, $(\rho, \rho u, \rho v, E_T)$. E_T is the total energy per unit volume which is given by

$$E_T = \rho[e + (u^2 + v^2)/2] \tag{2}$$

and e is the internal energy per unit mass. $\boldsymbol{F}$ and $\boldsymbol{G}$ are the inviscid, and $\boldsymbol{R}$ and $\boldsymbol{S}$ are the viscous flux vectors, respectively. The subscripts denote partial derivatives.

Received Feb. 24, 1992; presented as Paper 92-2508 at the AIAA 33rd Structures, Structural Dynamics and Materials Conference, Dallas, TX, April 13–15, 1992; revision received Jan. 26, 1993; accepted for publication March 10, 1993.

*Research Associate, Department of Aeronautics and Astronautics. Member AIAA.

†Professor, School of Aerospace Engineering, Georgia Institute of Technology. Member AIAA.

The above governing equations may be transformed into a general curvilinear coordinate system; $[\xi(x, y, t), \eta(x, y, t), \tau(t)]$. This transformation allows the solution of the equations on body-fitted, nonorthogonal computational grids. The transformed governing equations can also be expressed in the same conservative form as Eq. (1), however, the transformed flux terms are now related to their Cartesian counterparts through the metrics of transformation. For a detailed description of flux vectors in the Cartesian and transformed coordinate systems, the reader is referred to Ref. 9.

In the solution of the governing equations, boundary conditions are applied on the solid surfaces and the far-field boundaries. On the solid surfaces, the "no slip" condition is applied which simply states that the fluid velocity on the solid surface is equal to the velocity of the solid surface. In the case of a constant angle of attack, surface boundary velocities are set to zero. For oscillating airfoils, they are set to the solid surface velocities which are based on the reduced frequency of the motion. At the far-field boundary, freestream values of the flow variables are applied.

The turbulence in high Reynolds number flows is modeled by Reynolds stresses. Reynolds stresses are similar to the viscous stresses in that they contribute to the transport of momentum. They are similarly modeled as proportional to the strain. The eddy viscosity coefficient μ_t is employed as the proportionality constant. In this work, a two-layer Baldwin-Lomax eddy viscosity model is used. This model treats the eddy viscosity in two layers, inner and outer, and employs different length scales and empirical constants in each of these layers. For a detailed discussion of this model, the reader is referred to Ref. 9.

Although use of such a simple algebraic eddy viscosity model in massively separated flows may be questionable, earlier studies with higher order models[4] did not show any significant improvements in numerical predictions. Therefore, this model is employed in both separated flow and wake regions.

Numerical Method

The governing equations expressed in the transformed domain are first discretized and then integrated in time. Standard second-order accurate central differences are used to approximate the spacial derivatives, and to compute the metrics of transformation. The instabilities due to the growth of high-frequency errors in the numerical solution, which is caused by the odd-even coupling of the standard central differencing, are controlled by adding a set of artificial dissipation terms to the discretized equations. These dissipation terms consist of second- and fourth-order differences of the flow properties as suggested by Jameson.[10] The highly nonlinear inviscid flux terms in $\boldsymbol{F}$ and $\boldsymbol{H}$ are linearized about their values at a previous time level. The viscous flux terms are also evaluated at a previous time level and are applied explicitly on the right side of the governing equations. The resulting linear equations, which are expressed in delta quantity $(\boldsymbol{q}^n - \boldsymbol{q}^{n-1})$, form a

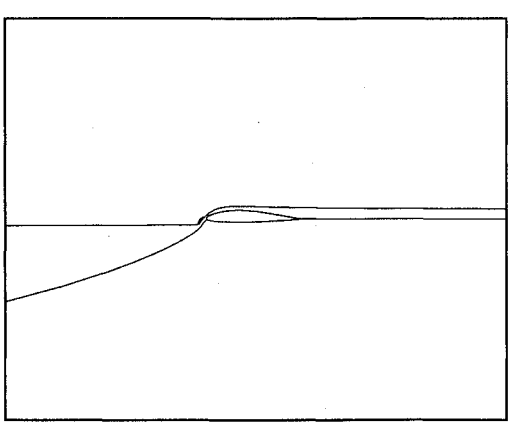

Fig. 1 Definition of a multiblock grid.

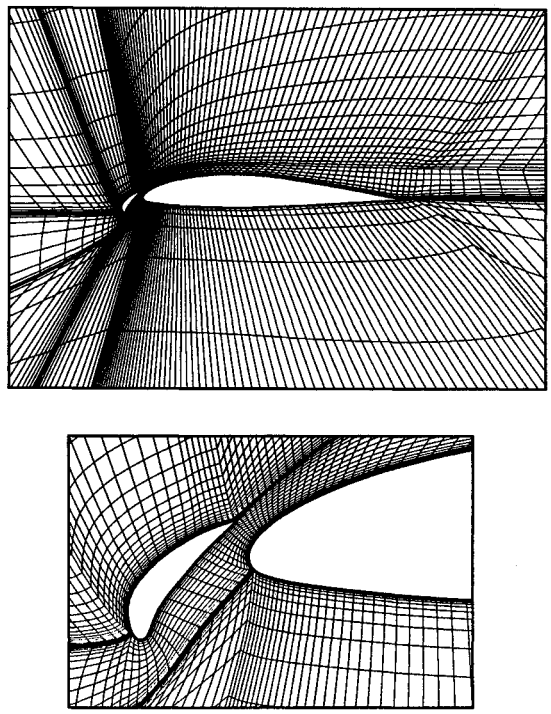

Fig. 2 a) Grid distribution near a slat/airfoil combination and b) a close-up view of the grid distribution around slat and airfoil leading edge.

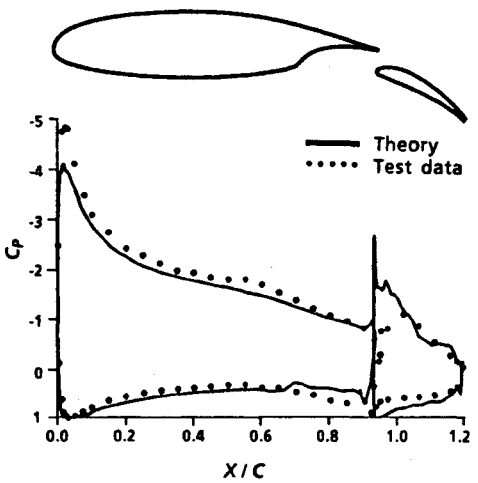

Fig. 3 Pressure distribution—GAW-130 airfoil, flap angle 20 deg, $M = 0.3$, $Re = 2.2 \times 10^6$.

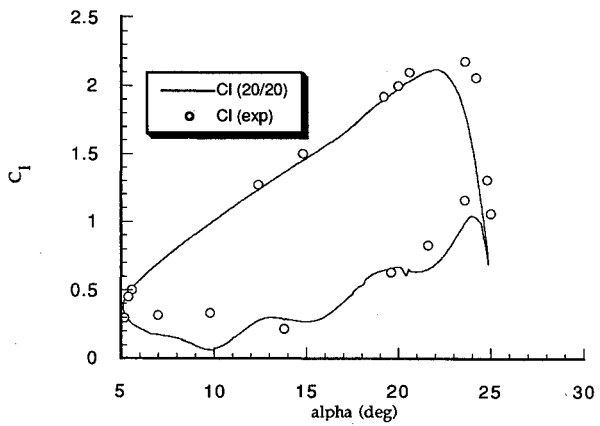

Fig. 4 Unsteady lift—oscillating NACA 0012 airfoil, $k = 0.151$, $M = 0.283$.

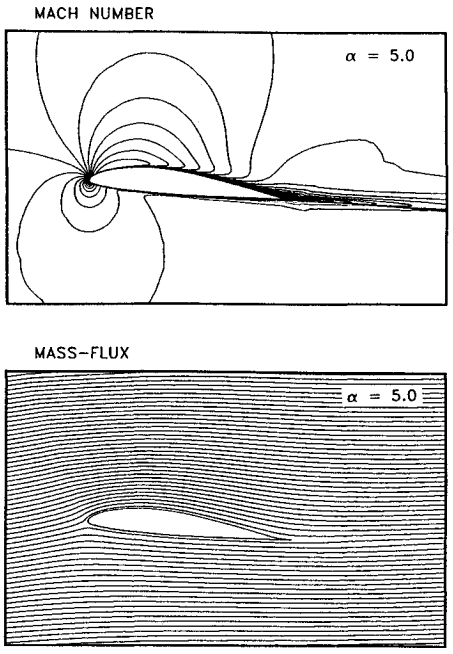

Fig. 5 Mach number and mass-flux contours—α = 5 deg, single element.

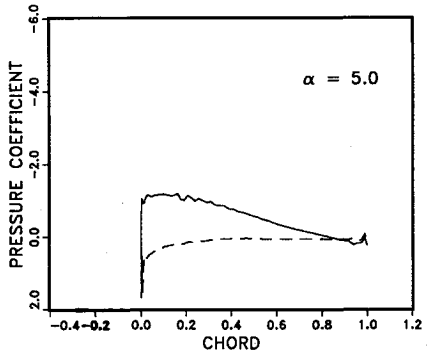

Fig. 6 Pressure distribution—α = 5 deg, single element.

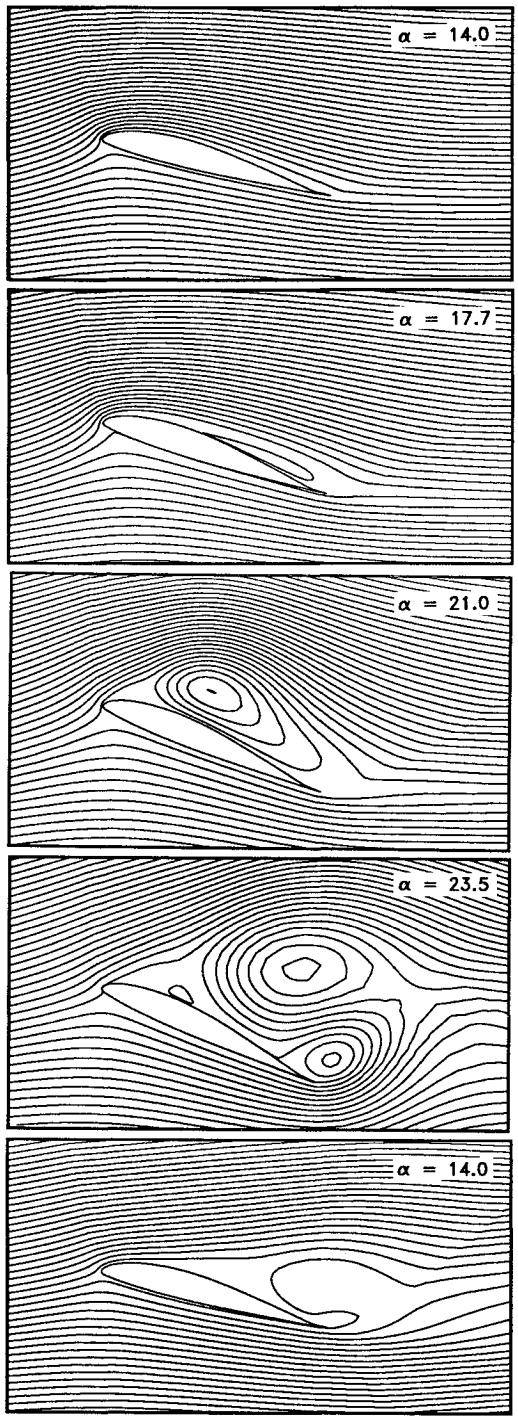

Fig. 7 Instantaneous mass-flux contours—α = 15–10 deg cos(ωt), single element.

penta-diagonal matrix system of simultaneous equations. For an efficient solution of these linear equations, the penta-diagonal matrix system is approximately factored into a product of tridiagonal matrices using the Beam-Warming approximate factorization scheme. The details of the numerical formulation are discussed in detail in Ref. 9.

The computational domain is discretized by employing multiple blocks and generating computational grids in each block. The governing equations are solved in each block as previously described. At the block interfaces, the continuity of the flow variables across the block boundaries is enforced. In the computation of eddy viscosity values, care is taken near the block boundaries in the direction normal to the solid surfaces so that inner and outer eddy viscosity values are computed across the block boundaries and assigned correctly.

Numerical solution of the discretized governing equations is based on the numerical integration of these equations in space and time. For a steady-state solution at a constant angle of attack, the flowfield is first initialized with the freestream and appropriate boundary conditions. Then, the equations are integrated by marching in time until a converged solution is reached. In steady flow computations, in which the final solution is independent of time, a local time step which varies in space may be used. Local time stepping increases the convergence rates and efficiency of the computations. In this study, we used a geometric variation of the time step Δt, proportional to the grid spacing

$$\Delta t = [\Delta T/(1 + \sqrt{J})] \tag{3}$$

where J is the Jacobian of the grid cell and $\sqrt{J}$ represents the width of the grid cell. ΔT is set to 1.

The computation of the unsteady flowfields takes a steady-state solution already computed as the initial condition. The equations are then integrated in time with a global, constant time step, which conserves the time accuracy of the solution. Unsteady boundary conditions are updated at every time step. The flow variables at the block boundaries are updated after every sweep by averaging the values at the first inner grid nodes next to the block boundary in neighboring blocks.

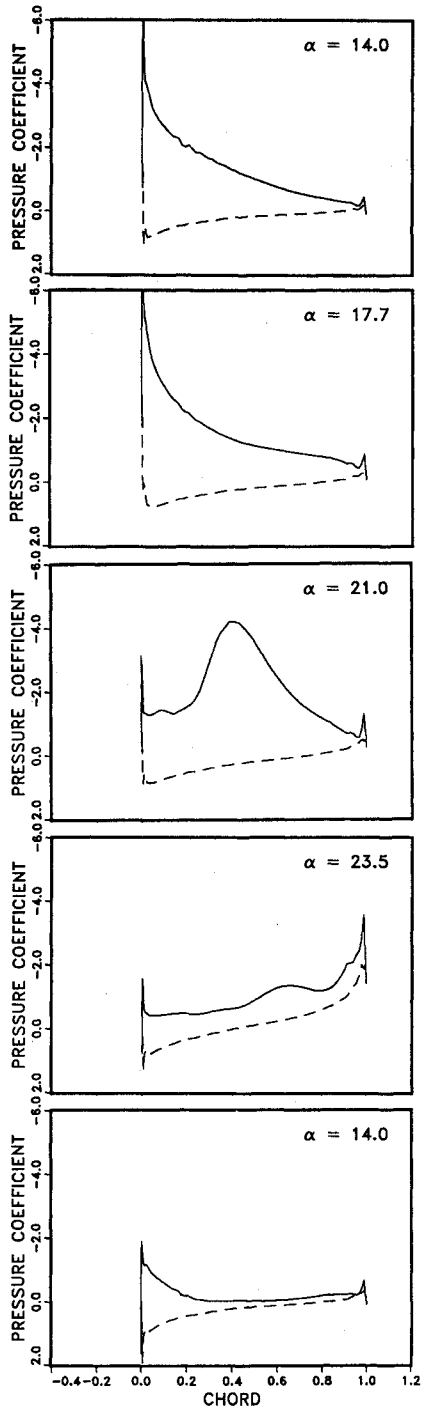

Fig. 8 Pressure distribution—α = 15–10 deg cos(ωt), single element.

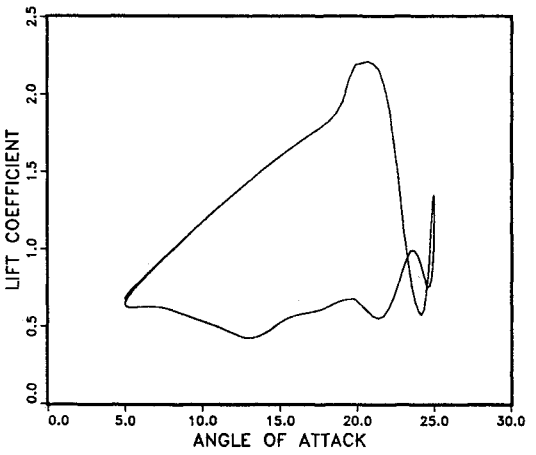

Fig. 9 Unsteady lift—α = 15–10 deg cos(ωt), single element.

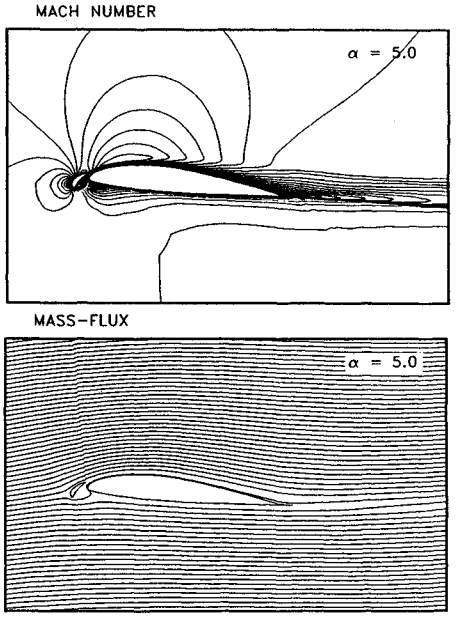

Fig. 10 Mach number and mass-flux contours—α = 5 deg, slat/airfoil.

The multiblock grid generation scheme is based on the division of a multiply connected computational domain into simple, simply connected rectangular blocks and the generation of a near orthogonal grid in each block individually. Airfoil profiles, block boundaries, and grid distribution along the block boundaries in terms of the first and the last grid spacing are user defined. With these given boundary conditions, an elliptic solver is employed for generating near orthogonal grids in each block. Grid spacing along the directions normal to the solid surfaces is then redistributed according to the first grid spacing off the solid surface specified as input. This procedure enables a sufficient number of grid points to be placed within the boundary-layer zone of the flow. Continuity of a global grid across block boundaries is satisfied by averaging the coordinates on either side of the common block boundaries.

Figure 1 shows the definition of blocks for a slat/airfoil combination. The distribution of grid points around the slat/airfoil combination and a close-up view of the leading-edge region are given in Figs. 2a and 2b. In Fig. 2a, only every other horizontal grid line is shown for clarity.

Numerical Results and Discussion

Previous Validation Studies

In the past, the present methodology has been used for a number of steady and unsteady flow problems, and some of the previously published work is reproduced here to demonstrate the ability of this technique. Figure 3 shows the steady surface pressure distribution computed over a GAW-130 airfoil/flap combination.[11] The total computed C_l value of 2.62 is in good agreement with the measured value of 2.67 for this case. Figure 4 shows the dynamic stall hysteresis loop for a single element NACA 0012 airfoil for a reduced frequency of 0.15 at M = 0.283.[12] Additional code validation studies are presented in Ref. 4.

Present Results

The finite difference methodology mentioned previously was applied to an oscillating single VR-7 airfoil as a baseline study. The calculations were then repeated for a leading-edge

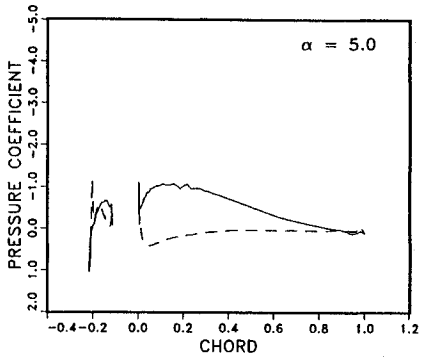

Fig. 11 Pressure distribution—α = 5 deg, slat/airfoil.

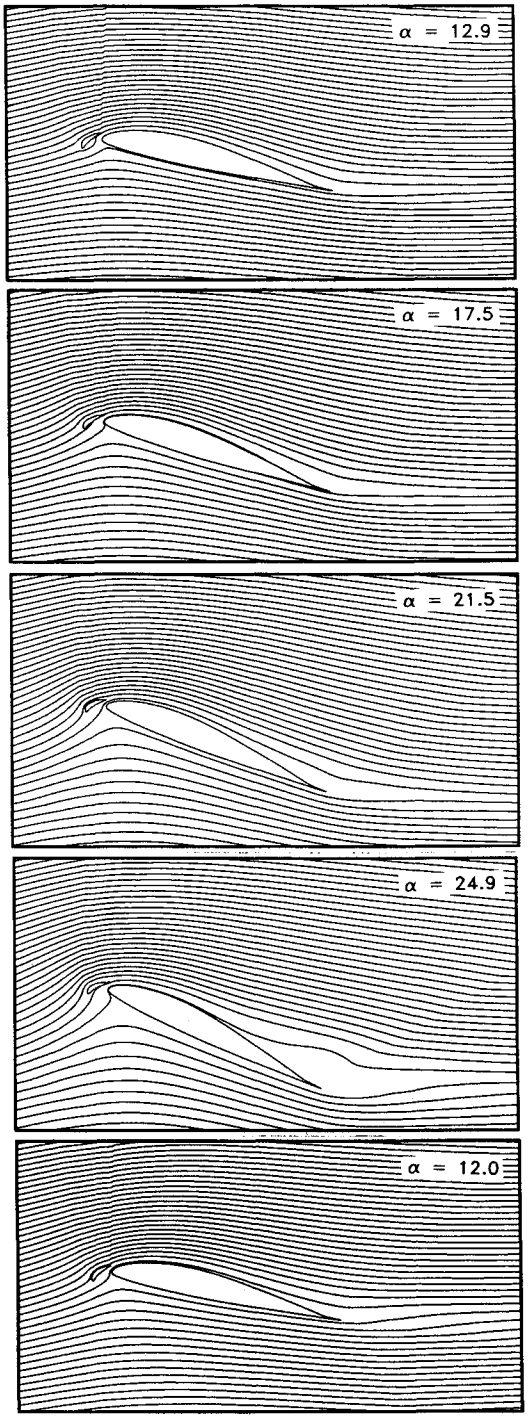

Fig. 12 Instantaneous mass-flux contours—α = 15–10 deg cos(ωt), slat/airfoil.

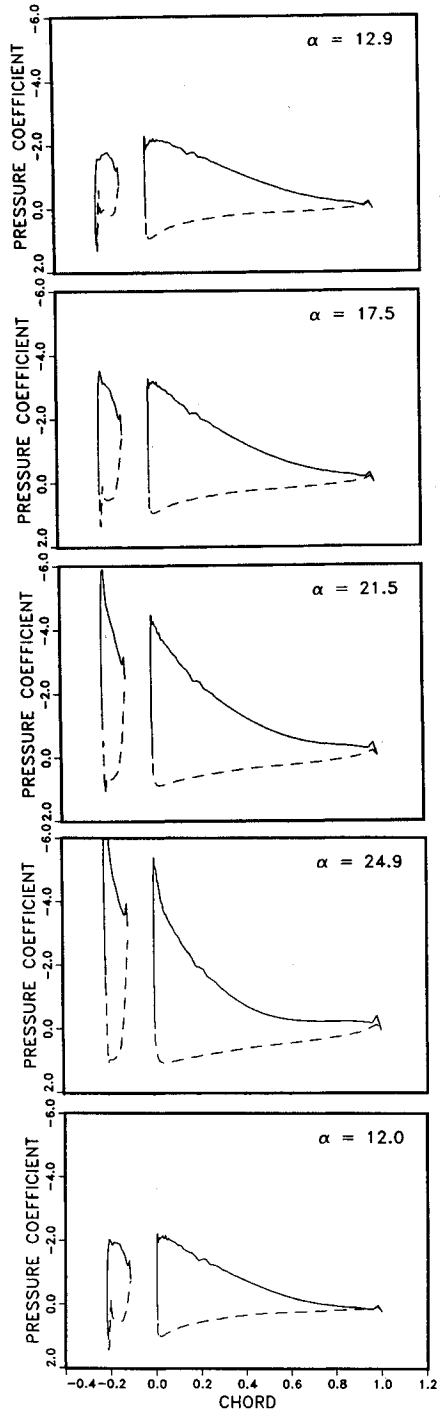

Fig. 13 Pressure distribution—α = 15–10 deg cos(ωt), slat/airfoil.

slat/airfoil combination. In these cases, the oscillatory pitching motion is about the quarter-chord of the main airfoil, and of a sinusoidal type described by α = 15–10 deg cos(ωt). The frequency of the motion ω is based on the nondimensional reduced frequency parameter k, which is defined as $k = \omega c/2U_\infty$. c is the chord length. For both the airfoil and the slat/airfoil combination, the unsteady flowfields and dynamic stall characteristics are computed at k = 0.10, $Re = 2.5 \times 10^6$, and M = 0.185. Unsteady flowfields over the VR-7 slat/airfoil configuration have also been tested at NASA by Carr and McAlister[2] for the flow conditions mentioned above.

Single Airfoil

In this case, two grid blocks with 121 × 58 and 121 × 41 in size on the upper and lower sides of the airfoil, respectively, were employed. One hundred twenty-eight grid points were

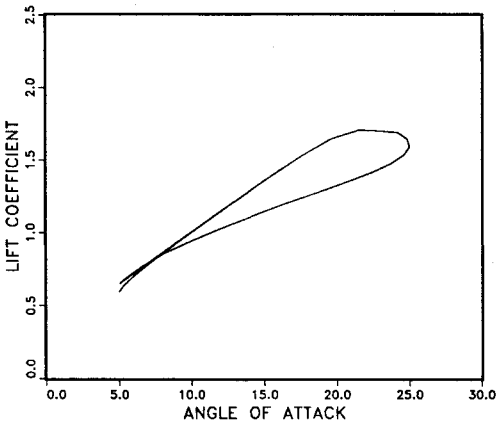

Fig. 14 Unsteady lift—α = 15–10 deg cos(ωt), slat/airfoil.

placed over the airfoil (upper and lower surfaces), and the first grid point was placed at 0.000005 chord length off of the solid surface boundary. The steady-state solution at α = 5 deg was obtained using a local time stepping. The computed flowfield in terms of Mach number and mass-flux contours around the airfoil is depicted in Fig. 5. The computed lift coefficient is 0.68, which compares well with the experimental value of 0.7.[1] Figure 6 shows the distribution of surface pressure.

The unsteady flowfield along the oscillatory motion was then computed by advancing this solution in time with time-dependent boundary conditions. The computed unsteady flowfields along the pitching motion is depicted in Fig. 7. Figure 8 also shows the corresponding distribution of the pressure coefficient around the airfoil. The variation of lift with respect to angle of attack is given in Fig. 9. It is seen that the flowfield stays mostly attached up to the static stall angle, which is about 14 deg. Separated flow regions and the formation of a vortex at the trailing edge is observed at around α = 17.7 deg $\uparrow$ (the $\uparrow$ sign denotes pitch-up). The flow separation consequently reaches the leading edge, and a completely separated vortical region covers the upper surface. A strong suction peak is induced on the upper airfoil surface by the vortex as observed in the pressure distribution. At this stage, before the vortex starts moving off the airfoil surface and the vortex induced suction decreases, the maximum lift equal to 2.21 is attained at α = 20.6 deg $\uparrow$. As the angle of attack increases further, the main vortex lifts off the surface and is shed into the wake. The lift drops drastically and the airfoil stalls. In addition to a secondary, weak trailing-edge vortex, local suction peaks in the pressure distribution reveal the presence of weak vortical structures. However, the secondary trailing-edge vortex is also shed into the wake and the pressure distribution on the upper surface flattens out subsequently.

The flowfield remains mostly separated along the return cycle. Around α = 14 deg $\downarrow$, the flow reattachment starts from the leading edge downward. However, the aerodynamic lift stays well below the attached flow values attained during the pitch-up. The lift finally recovers back to attached flow values as the minimum angle of attack is reached and the second pitch-up cycle starts.

Slat/Airfoil Combination

In this case, the computational grid consisted of three blocks with 121 × 49, 121 × 29, and 121 × 31 points from the top to the bottom, as seen in Fig. 1. One hundred twenty-eight grid points over the main airfoil surface and forty points over the slat were placed. The steady-state solution is depicted in Fig. 10. The pressure distribution on the slat and the airfoil is given in Fig. 11. It should be noted that the suction peak at the leading edge of the airfoil is not as pronounced as it is in the single airfoil case. The lift coefficient on the main airfoil was found to be 0.59. This may be attributed in part to the downwash over the main airfoil caused by the bound circulation around the slat.

The computed unsteady flowfields and the corresponding pressure distributions are given in Figs. 12 and 13. It is readily observed that the massive flow separation experienced in the single airfoil does not occur. The flowfield stays attached well beyond the static stall angle of the single airfoil. As the maximum angle of attack is reached, the thickened boundary layer over the upper surface separates at the trailing edge. However, the separated region is confined to the rear portion of the airfoil and it does not progress towards the leading edge. The lack of a suction peak on the upper surface around the trailing edge also suggests that a trailing-edge vortex does not form.

In comparison to the single airfoil case, the suction peak values at the leading edge at around α = 15 deg $\uparrow$ are smaller. The fact that the adverse pressure gradient is not as large may explain the delayed separation of the flow. On the other hand, the suction peaks reached at around the maximum angle of attack is quite comparable to the maximum values experienced in the single airfoil case prior to the flow separation. Yet, the flow at the leading edge still stays attached. It may be argued at this point that the accelerated flow over the slat energizes the boundary layer on the main airfoil, and prevents it from being separated.

The variation of lift coefficient on the main airfoil is given in Fig. 14. It is also clearly seen that the dynamic stall is completely eliminated. It may be noted that experimental load data for VR-7 slat/airfoil combination given by Carr et al.[2] was measured on the main airfoil alone. It is reported that these loads were corrected to match the lift-curve slope of the basic airfoil.[2] Since rationale for such adjustments is not clear in an unsteady flow environment, these measured data are not included in the present study.

Concluding Remarks

A numerical procedure for the computation of the dynamic stall characteristics of multielement airfoils has been developed and applied to a VR-7 slat/airfoil configuration. The computations clearly demonstrate the beneficial effects of slat on the airfoil loads at very large angles of attack.

This method may be used in systematic studies of slat shape, slat clearance, etc., needed in the aerodynamic design of high-lift devices. The two-dimensional static and dynamic loads computed in this work may also be used in helicopter performance analyses (such as CAMRAD) as table look-up values to assess the effects of slat on rotor performance and vibrating airloads.

Acknowledgments

This work was supported by NADC under Contract N62269-90-C-0246. The authors would like to thank Dave Findlay for his stimulating interest in this work.

References

[1]McCroskey, W. J., McAlister, K. W., Carr, L. W., and Pucci, S. L., "An Experimental Study of Dynamic Stall on Advanced Airfoil Sections," Vols. 1–2, NASA TM 84245, July 1982.

[2]Carr, L. W., and McAlister K. W., "The Effect of a Leading-Edge Slat on the Dynamic Stall of an Oscillating Airfoil," AIAA Paper 83-2533, Oct. 1983.

[3]Tuncer, I. H., Wu, J. C., and Wang, C. M., "Theoretical and Numerical Studies of Oscillating Airfoils," *AIAA Journal*, Vol. 28, No. 9, 1990, pp. 1615–1624.

[4]Wu, Jiunn-Chi, Huff, D., and Sankar, L. N., "Evaluation of Three Turbulence Models in Static Airloads and Dynamic Stall Predictions," *Journal of Aircraft*, Vol. 27, No. 4, 1990, pp. 382–384.

[5]Dutt, H. N. V., "Analysis of Multi-Element Airfoils by Vortex Panel Method," *AIAA Journal*, Vol. 27, No. 5, 1989, pp. 658–660.

[6]Hall, I. M., and Suddhoo, A., "Inviscid Compressible Flow Past a Multi-Element Aerofoil," AGARD-CP-365, Aug. 1984.

[7]Wang, C., Wu, J. C., and Tung, C., "A Numerical Study of General Viscous Flows Around Multi-Element Airfoils," AIAA Paper 90-0572, Jan. 1990.

[8]Sankar, L. N., and Tang, W., "Numerical Solution of Unsteady Viscous Flow Past Rotor Sections," AIAA Paper 85-0129, Jan. 1985.

[9]Wake, B. E., "Solution Procedure for the Navier-Stokes Equations Applied to Rotors," Ph.D. Dissertation, School of Aerospace Engineering, Georgia Inst. of Technology, Atlanta, GA, April 1987.

[10]Jameson, A., Schmidt, W., and Turkel, E., "Numerical Solution of the Euler Equations by Finite Volume Methods Using Runge-Kutta Time Stepping Schemes," AIAA Paper 81-1259, June 1981.

[11]Narramore, J. C., and Sankar, L. N., "Numerical Simulation of Multizone Two-Dimensional Transonic Flows Using the Full Navier-Stokes Equations," International Technical Specialists' Meeting on Rotorcraft Basic Research of the American Helicopter Society, Georgia Institute of Technology, Atlanta, GA, March 1991.

[12]Hixon, R., and Sankar, L. N., "Minimal Residual Method for Application of a Generalized Two-Dimensional Unsteady Flow," AIAA Paper 92-0430, Jan. 1992.